Published in final edited form as:
Nanomedicine (Lond). 2012 December ; 7(12): 1827–1837. doi:10.2217/nnm.12.92.

A nano-sized PARACEST-fluorescence imaging contrast agent facilitates & validates *in vivo* CEST MRI detection of glioma

Meser M Ali[1,*], **Mohammed PI Bhuiyan**[1], **Branislava Janic**[1], **Nadimpalli RS Varma**[1], **Tom Mikkelsen**[1], **James R Ewing**[1], **Robert A Knight**[1], **Mark D Pagel**[2], and **Ali S Arbab**[1]

[1]Henry Ford Hospital, Detroit, MI 48202, USA

[2]Arizona Cancer Center, University of Arizona, Tucson, AZ 85724, USA

Abstract

Aim—The authors have investigated the usefulness of *in vivo* chemical exchange saturation transfer MRI for detecting gliomas using a dual-modality imaging contrast agent.

Materials & methods—A paramagnetic chemical exchange saturation transfer MRI contrast agent, Eu-1,4,7,10-tetraazacclododecane-1,4,7,10-tetraacetic acid-Gly_4 and a fluorescent agent, DyLight® 680, were conjugated to a generation 5 polyamidoamine dendrimer to create the dual-modality, nano-sized imaging contrast agent.

Results—The agent was detected with *in vivo* chemical exchange saturation transfer MRI in an U87 glioma model. These results were validated using *in vivo* and *ex vivo* fluorescence imaging.

Conclusion—This study demonstrated the merits of using a nano-sized imaging contrast agent for detecting gliomas and using a dual-modality agent for detecting gliomas at different spatial scales.

Keywords

brain tumor; contrast agent; dendrimer; MRI; pharmacokinetic

Exogenous, relaxivity-based MRI contrast agents are often used to improve image contrast by altering the T1, T2 and/or T2* relaxation rates of tissues [1]. Similarly, fluorescent contrast agents can also generate high-contrast images [2]. These exogenous agents can improve diagnostic sensitivity for detecting pathological lesions that have abnormal pharmacokinetic rates of accumulating the agents, relative to normal tissues. However, all tissues have endogenous magnetic resonance (MR) relaxation contrast mechanisms and also produce auto-fluorescence. All vascularized tissues are capable of accumulating contrast

*Author for correspondence: Tel.: +44 313 874 4479, Fax: +44 313 874 4494, mesera@rad.hfh.edu.

Ethical conduct of research

The authors state that they have obtained appropriate institutional review board approval or have followed the principles outlined in the Declaration of Helsinki for all human or animal experimental investigations. In addition, for investigations involving human subjects, informed consent has been obtained from the participants involved.

Financial & competing interests disclosure

This work is supported by the National Institutes of Health through grants K25CA129173, R21NS066143, R01CA122031 and P50 CA95060. The authors have no other relevant affiliations or financial involvement with any organization or entity with a financial interest in or financial conflict with the subject matter or materials discussed in the manuscript apart from those disclosed.
No writing assistance was utilized in the production of this manuscript.

agents. Thus, normal tissues with abnormal contrast may be mistaken for pathological lesions, so MRI and fluorescence imaging can suffer from poor diagnostic specificity.

Within the last decade, a new class of MRI contrast agents has been developed, which depend on the mechanism of chemical exchange saturation transfer (CEST) [3]. These agents possess a chemical functional group with a labile proton, such as an amide or hydroxyl group, that has a MR frequency (chemical shift) that differs from the chemical shift of water by approximately 1–5 ppm. Selective radio frequency saturation of the chemical shift of the labile proton eliminates the MR signal from the proton in the sample. The subsequent exchange of this proton with a proton on a water molecule effectively transfers the saturation to water, which reduces the MR signal from water in the sample. The CEST effect was first demonstrated with small diamagnetic molecules, such as amino acids, sugars, nucleic acids and heterocyclic ring compounds [4]. To improve the difference in chemical shifts between the agent and water, metal ions have been incorporated into chemical structures to create paramagnetic CEST (PARACEST) agents [5,6]. Some PARACEST agents have been designed to noncovalently bind to a water molecule. For example, Eu-1,4,7,10-tetraazacclododecane-1,4,7,10-tetraacetic acid (DOTA)-Gly_4 can generate CEST via the bound water [5].

PARACEST agents have strong potential to improve the specificity of MRI diagnoses. For instance, the chemical exchange of amide protons is base-catalyzed and therefore PARACEST agents with amides can be used to measure pH and detect tumor acidosis, which may improve specificity for detecting tumors relative to normal tissues [7,8]. Furthermore, CEST agents that can detect the activities of tumor protease enzymes by monitoring the conversion of amides to amines during peptide cleavage have been developed, which may further improve diagnostic specificity [9–11]. Additionally, CEST agents can detect metabolites such as nitric oxide, which is an important paracrine signaling messenger for promoting tumor angiogenesis, and can further improve diagnostic specificity [12]. Importantly, the ability to selectively detect multiple PARACEST agents during a single MRI scan session may provide the ability to evaluate multiple biomarkers, which may multiply the specificity of tumor detection with MRI [13].

Unfortunately, PARACEST agents have relatively poor detection sensitivity. As a rough estimate, a detectable CEST effect that saturates 1% of approximately 110 M water protons requires approximately 10 mM of a PARACEST agent, with one labile proton and a chemical exchange rate of approximately 100 Hz. Small molecule PARACEST agents with multiple labile protons at the same chemical shift and/or with faster chemical exchange rates can generate a detectable CEST effect at concentrations of approximately 1 mM in chemical solutions (note: a faster exchange rate cannot exceed the chemical shift difference between the agent and water, otherwise the CEST effect will be decreased) [3]. However, this minimum concentration (1 mM) of exogenous PARACEST agents is not suitable for *in vivo* studies, because endogenous proteins have labile protons that generate a magnetization transfer effect that is similar to CEST, which competes with the CEST agents for exchange with water [14]. To date, few reports have demonstrated *in vivo* detection of exogenous small molecule PARACEST agents [7,8,13,15–21].

To improve *in vivo* detection sensitivity, PARACEST agents have been conjugated to nanocarriers such as dendrimers, linear polymers and other high molecular weight macromolecules, such as adenovirus particles [22–24]. For example, the authors have previously conjugated an Eu-DOTA-Gly_4 PARACEST agent to a generation 5 polyamidoamine (G5PAMAM) dendrimer via 1-ethyl-3-(3-dimethylaminopropyl) carbodiimide/*N*-hydroxysuccinimide (NHS) coupling, and demonstrated that injection of the agent into a mouse model of mammary carcinoma generated CEST in tumor tissue [17].

Although this preliminary result showed that the CEST image contrast was statistically significant, the result was not validated using other methods, which raised concern that the change in image contrast may have originated from conditions other than the CEST agent, such that the agent had not necessarily accumulated in the tumor tissue. Other conditions that may dynamically change image contrast, include T2 relaxation effects, endogenous magnetization transfer or magnetic susceptibility that affects the direct saturation of water. Similarly, all other *in vivo* MRI studies with PARACEST agents that have been published to date have not been validated using other imaging methods [7,8,13,15–21].

Dual-modality contrast agents are ideally suited for the validation of imaging results, because the conditions that may confound the interpretation of one imaging modality rarely affect the other. Furthermore, a dual-modality contrast agent can be designed to exploit the strengths of two complimentary imaging modalities, which can multiply the value of the agent for biomedical imaging [25]. MRI is often used for presurgical planning to identify the macroscopic features of pathological tissues, and fluorescence imaging is emerging as a useful intrasurgical tool to identify microscopic margins of pathological tissues [26,27]. Therefore, conjugating fluorescent agents and PARACEST agents to a dendrimer is a synergistic approach.

In order to validate the *in vivo* detection of a PARACEST agent, the authors investigated the development of a fluorescent PARACEST MRI contrast agent using a G5PAMAM dendrimer as the nanocarrier (Figure 1). The author and colleagues used a rat model of U87 human glioma for the *in vivo* study, in order to apply their imaging methods to a major diagnostic problem [28]. The accumulation of a nano-sized imaging agent in a hypervascular glioma can improve diagnostic specificity by distinguishing the glioma from peritumoral edema [29]. The glioma can compromise the blood–brain barrier and allow accumulation of polar, nano-sized contrast agents that are typically impermeable to this barrier, which further improves diagnostic specificity for detecting the tumor [30]. Therefore, the development of a nano-sized, dual-modality MRI contrast agent may have excellent utility for the diagnoses of gliomas, especially the tumor margin, and may improve treatment planning.

Materials & methods

Synthesis of Eu-DOTA-Gly$_4$

DOTAM-Gly, the tetraglycineamide derivative of DOTA, was synthesized using a previously reported method in [6]. Unless otherwise noted, all reagents were purchased from Acros Organics (Geel, Belgium), or Sigma-Aldrich Inc. (MO, USA), and used without further purification. DN-(2-Bromoethanoyl) ethyl glycinate was synthesized from bromoethanoyl bromide (10.5 ml, 120 mmol) and glycine ethyl ester (14 g, 100 mmol). DOTAM-Gly-OEt was synthesized through exhaustive alkylation of cyclen (1,3,5,7-tetraazacyclododecane; 1.72g, 10 mmol) with *N*-(2-bromoethanoyl) ethyl glycinate (9.19 g, 41 mmol) in acetonitrile with K_2CO_3 (11.06 g, 80 mmol) at 70°C for 6 h under N_2 gas. After the reaction, undissolved materials were removed by filtration and the final product was obtained by evaporating the solvent (7.40 g, quantitative yield). The hydrolysis of DOTAM-Gly-OEt (7.45 g, 10 mmol) was conducted in ethanol:water (1:1) at 60°C by controlling pH at approximately 11 with 1 N-NaOH. The 1-h reaction was traced with thin-layer chromatography. The reaction mixture was cooled, acidified to pH 3 with 1 N-HCl, lyophilized, redissolved in water, and purified with liquid chromatography (solid-phase: Amberlite® XAD-1600; eluent: water, 5.04 g, 80% yield).

Synthesis of [Eu-DOTA-Gly_4]$_{42}$–G5PAMAM

A G5PAMAM dendrimer (Dentritech Inc.; MI, USA) was labeled with Eu-DOTA-Gly_4 using the method previously published in [17]. Briefly, NHS (0.21 g, 1.83 mmol) and 1-ethyl-3-(3-dimethylaminopropyl) carbodiimide.HCl (0.88 g, 4.6 mmol) was added to a stirred solution of Eu-DOTA-Gly_4 (0.81 g, 1.03 mmol) in 2-(*N*-morpholino)ethanesulfonic acid buffer (20 ml, pH 6.5) at 0°C for 1 h. The resulting active ester, Eu-DOTA-Gly_4 NHS, was added in aliquots to a stirred solution of G5PAMAM dendrimer (0.08 g, 72 μmol) in 3.5 ml of phosphate-buffered saline (PBS) at pH 7.4 and then allowed to stir at room temperature for 24 h. The solution was filtered using a centrifugal filter unit with a 10,000 molecular weight cut-off (Millipore Inc., MA, USA). Finally, the solution was lyophilized to obtain 420 mg of a white solid, which represented a 17% yield. Matrix-assisted laser desorption/ionization mass spectrometry was used to characterize the average number of DOTA-Gly_4 ligands conjugated to G5PAMAM.

Synthesis of [DyLight® 680]$_1$– [Eu-DOTA-Gly_4]$_{42}$–G5PAMAM

A solution of DyLight 680 NHS ester (50 mg, ~0.071 mmol; Thermo Fisher Scientific, IL, USA)) in dimethyl sulfoxide was added to a stirred solution of Eu-G5PAMAM (200 mg, 0.071 mmol) in 2 ml of PBS, and the reaction was stirred at room temperature for 24 h. The reaction mixture was diafiltrated using Amicon Ultra centrifugal filter unit with a 10,000 molecular weight cut-off. The solution was lyophilized to obtain 210 mg of solid (~066 mmol, 93% yield). The emission profile of the final product was determined and compared with that of DyLight 680.

Synthesis of [DyLight 680]$_1$-G5PAMAM

The same procedure used to label Eu-G5PAMAM with a fluorophore was used to label a G5PAMAM dendrimer. A solution of DyLight 680 NHS ester (150 mg, 0.16 mmol) in dimethyl sulfoxide was added to a stirred solution of G5PAMAM dendrimer (0.040 g, 1.3 mmol) in 2 ml of PBS, and the reaction was stirred at room temperature for 24 h. The reaction mixture was diafiltrated using Amicon Ultra centrifugal filter unit with a 10,000 molecular weight cut-off. The solution was lyophilized to obtain 0.041 g of solid (~1.4 mmol, 87% yield). The emission profile of the final product was determined and compared with that of DyLight 680.

Animal model

The animal study was conducted according to approved procedures of Institutional Animal Care and Use Committee of Henry Ford Hospital (MI, USA). U87 human glioma cells were provided by Tom Mikkelsen from the Henry Ford Hospital. The cells were cultured in 75 cm^2 tissue culture flasks with DMEM supplemented with 10% fetal bovine serum, penicillin (100 IU/ml) and streptomycin (100 μg/ml) until they were 80–90% confluent. The cells were collected by trypsinization, washed and centrifuged to make a cell suspension of 4 × 105 cells/5 μl.

An athymic nude rat that was 6–8 weeks old and weighed 160 g (Charles River Laboratory Inc., MD, USA) was anesthetized by intraperitoneal injection, using a mixture of 100 mg/kg ketamine and 15 mg/kg xylazine. Orthotopic human glioma was created in nude rats by implanting 4 × 105 human U87 glioma cells according to a recently published method in [31]. The orthotopic tumor was allowed to grow for 4–5 weeks to a diameter of approximately 5–7 mm, before conducting the MRI study.

In vitro CEST MRI studies

Solutions of DyLight 680-Eu-G5PAMAM that ranged in concentration from 46.9–2750 μM (on a per dendrimer basis) were prepared in PBS at pH 7. The concentrations of these solutions were validated using inductively coupled plasma mass spectrometry. Images were acquired using a 7T Varian MR scanner that was equipped with a 12-cm bore magnet and a 38-mm diameter homemade transmit/receive quadrature birdcage coil. The CEST effects of these samples were measured at 37°C using a rapid acquisition with refocused echoes pulse sequence (echo time: 5 s; repetition time: 10 ms; rapid acquisition with refocused echoes factor: 8; one image slice at 2-mm slice thickness; 128 × 128 matrix, 250 × 250 μm in-plane resolution; 24 × 24 mm field of view; one average) [16]. This experiment was prepended with a selective saturation pulse applied at 17 μT for 1.6 s at MR frequencies ranging from +80 to −60 ppm in 1 ppm increments (where the water resonance is referenced to 0 ppm). This saturation time and saturation power was considered to generate a maximum CEST effect, because a saturation time of 2 s and a saturation power of 20 μT produced the same CEST effects. The percent CEST was calculated by comparing the images acquired with selective saturation at +55 ppm (M_S) with images acquired with selective saturation at −55 ppm (M_0) (equation 1). Image contrast was measured using ImageJ (NIH, MD, USA), and the calibration of the CEST effect with respect to concentrations was evaluated using a Hanes-like linear analysis method, which was evaluated with MS Excel (Microsoft Inc., MI, USA).

$$\%CEST = \frac{M_0 - M_s}{M_0}$$

In vivo CEST MRI studies

The same Varian MRI scanner used for *in vitro* studies was also applied for the *in vivo* study. To prepare for the MRI scans, the rat was initially anesthetized with 3.0% isoflurane in a 2:1 N_2O:O_2 mixture administered via a facemask, followed by 1.2–2.0% isoflurane during the MRI scans. The respiration rate and rectal temperature were continuously monitored using an automated feedback system (SA Instruments Inc., NY, USA). During MRI studies, the rectal temperature was automatically maintained at 37.0 ± 0.2°C using warmed air. The rat was secured in a customized MRI-compatible cradle to prevent injury during the MRI exam and to stabilize the head with ear bars in order to eliminate motion artifacts during MRI scans.

An isotropic 3D fast imaging employing steady state acquistion MR image was acquired to locate the U87 glioma in the rat model using 3T GE Excite clinical MRI system fitted with dedicated small animal coil (Litzcage small animal imaging system, Doty Scientific Inc., SC, USA) [31]. The fast imaging employing steady state acquistion images were obtained with the following parameters – echo time: 11.4 ms; repetition time: 5.61 ms; 0.3-mm slice thickness; 200 × 200 matrix; 300 × 300 μm in-plane resolution; 60 × 60 mm field of view and; two averages. The tumor rim was visualized by thresholding the image to obtain a contiguous loop of pixels that had the lowest signal amplitude in the region of the glioma. This tumor rim was used to define the region of interest for subsequent analyses.

The same CEST–rapid acquisition with refocused echoes MRI protocol used for *in vitro* studies was also applied for the *in vivo* study, except that a 32 × 32 mm field of view was used. This protocol provided a 80-s temporal resolution that did not cause sample heating. A series of axial images with saturation frequencies applied at +55 ppm were acquired for 48 min. After the first six images were acquired, a solution of 0.045 mmol/kg DyLight 680-Eu-

G5PAMAM was injected through the tail vein catheter in 600 μl volume, which equated to a concentration of 12 mM that was prepared using the average molecular weight of DyLight 680-Eu-G5PAMAM, determined from matrix-assisted laser desorption/ionization mass–mass spectrometry analysis. This injection was prepended by injection of 100 μl heparinized saline and followed by 100 μl of saline to flush the catheter. The total volume of 800 μl was manually injected within approximately 1 min. Following MRI, the rat was moved to another facility for optical imaging.

The % CEST was calculated by comparing the average water signal at each post-injection time-point (M_S) with the water signal of the tumor determined from the average of the images acquired before injection (M_0) (Equation 1). The average water signal was obtained from the region of interest that was determined from the 3D FIESTA MRI study. The standard deviations of the CEST measurements were determined from the pixel-wise distributions of water signals in the region of interest. The contrast:noise ratio, or the CEST:noise ratio in this type of experiment, must exceed $2\sqrt{2}$ in order to ensure that the contrast has a 95% probability of being real [16]. Although this statistical threshold for the CEST:noise ratio is based on Rician noise, this threshold is also valid for Gaussian noise present in this study due to the high signal:noise ratio of 133:1 for the MR image of the tumor before injection. To determine the noise level, the standard deviation of the MR signal of an image region that represented air was multiplied by $\sqrt{2}$ to account for the subtraction of two images before and after injection. Only pixels that reached this CEST:noise threshold were used for subsequent analyses.

Optical imaging

Near-infrared fluorescence imaging of the rat was performed after acquisition of the MR images using a Kodak Carestream Multispectral Imaging System (Carestream, NY, USA). To obtain an optimal emission image devoid of nonspecific fluorescent emission, fluorescence images were acquired using multiple excitation wavelength filters, ranging from 540 to 690 nm and a single emission wavelength filter of 750 nm. Spectral profiles were created using the spectral analysis software (Carestream), from which subtracted optimal images were obtained. For each optical image set, an x-ray image was also obtained to validate the anatomic location of the tumor using the same animal position and field of view (the near-infrared and x-ray images were coregistered).

After *in vivo* imaging, the rat was euthanized using CO_2 asphyxiation and perfused by intracardiac injection of 100 ml PBS followed by 3% paraformaldehyde, and then kept in a solution of 3% sucrose and 3% paraformaldehyde during storage [31]. An *ex vivo* fluorescence image of the whole brain was acquired, which was registered to the *in vivo* fast imaging employing steady state acquistion MR image by comparing the outline of the autofluorescence and MR signal of the normal brain tissue. The brain was snap-frozen and cut into 15–20 μm thick sections for further analysis with fluorescence microscopy. For fluorescent microscopic detection of DyLight 680 conjugated to Eu-G5PAMAM, a proper excitation and emission filter was used. Sections were stained with fluorescein isothiocyanate-labeled tomato lectin to delineate endothelial lining of functional and nonfunctional blood vessels (neovascularization) [31]. Nuclei were visualized with 4′,6-diamidino-2-phenylindole (Sigma-Aldrich), using standard histological staining procedures as recommended by the suppliers of the reagent.

Results & discussion

Synthesis

The PARACEST agent, Eu-DOTA-Gly_4, was coupled to the G5PAMAM dendrimer by using Eu-DOTA-Gly_4 NHS ester, to perform an 1-ethyl-3-(3-dimethylaminopropyl)

carbodiimide/ NHS coupling method to form the PARACEST dendrimer Eu-G5PAMAM with a moderate 17% yield (Figure 1). The mass spectrum showed that an average of 42 Eu-DOTA-Gly_4 ligands were conjugated to the G5PAMAM dendrimer. Multiple carboxylates of the Eu-DOTA-Gly_4 ligands were activated during synthesis, which may have led to the conjugation of one Eu-DOTA-Gly_4 ligand to multiple amine end groups of the dendrimer. An average of 42 Eu-DOTA-Gly_4 ligands per dendrimer suggests that each Eu-DOTA-Gly_4 was conjugated to three amine end groups. This mass spectrum also showed a low, broad feature at approximately twice the mass-to-charge ratio of the main peak, which indicated a low level of dimerization of some dendrimers. This dimerization may have resulted from activation of multiple carboxylates of the Eu-DOTA-Gly_4 ligands, although the low level of dimerization suggests that the dilute conditions during synthesis minimized this problem.

The fluorescent agent, DyLight 680, was coupled to Eu-G5PAMAM, to form DyLight 680-Eu-G5PAMAM, with a high 93% yield. The mass spectrum showed an average of one DyLight 680 ligand per dendrimer. The same procedure was used to couple DyLight 680 to a G5PAMAM dendrimer without the PARACEST agent, which also resulted in an average of one fluorophore per dendrimer.

In vitro CEST MRI

The dual-modality contrast agent, DyLight 680-Eu-G5PAMAM, showed a large CEST effect at +55 ppm (Figure 2a). The CEST spectrum of DyLight 680-Eu-G5PAMAM was identical to the CEST spectra of Eu-G5PAMAM [ali *et al*, unpublished data] and was comparable to Eu-DOTA-Gly_4 [32]. Small ‘bumps’ at approximately -50, -30, 30 and 70 ppm in the CEST spectrum were attributed to pulse imperfections that the authors have observed in similar CEST MRI studies [8]. CEST from the primary amines and amides within the dendrimer may have also created CEST at these large chemical shifts. However, these other chemical groups would have to possess very slow or very fast exchange rates to create small ‘bumps’ relative to the large CEST effect at +55 ppm, which seems unlikely.

The concentration dependence of CEST for this agent (Figure 2b) showed an excellent fit to a two-pool model using a Hanes-like linear analysis method (Figures 2C & 2d). The PARACEST dendrimer, Eu-G5PAMAM, also showed CEST at +55 ppm and a similar fitting to the Hanes-like method (as determined from [17]). These results demonstrated that the presence of the fluorescent agent on DyLight 680-Eu-G5PAMAM did not affect the agent’s ability to generate CEST. In addition, Eu-G5PAMAM and DyLight 680-Eu-G5PAMAM each generate a 1% CEST effect with 14 μM on a PARACEST agent basis. For comparison, 530 μM of the small molecule PARACEST agent, Eu-DOTA-Gly_4, is needed to generate a 1% CEST effect under identical conditions (as determined from [17]). Therefore, coupling 42 PARACEST agents to the dendrimer resulted in a 38-fold improvement in sensitivity (on a per dendrimer basis), which shows that the CEST effect almost exactly scaled with the concentration of the agent on the dendrimer.

In vitro optical imaging

Conjugation of Dylight 680 to Eu-G5PAMAM shifted the absorption maximum (l_{abs}) and fluorescence emission maximum (l_{em}) of the fluorescent agent by 10 nm, relative to the corresponding bands for the free dye (Figure 3). This red shift is consistent with conjugation of a fluorescent dye to a nanocarrier [33]. Quenching was not observed from the fluorescence emission of DyLight 680 in DyLight 680-Eu-G5PAMAM, relative to the fluorescence emission of the free dye. This result confirmed that potential fluorescence quenching originating from Eu(III) was negligible, therefore, the presence of the PARACEST agent on DyLight 680-Eu-G5PAMAM did not affect the agent’s ability to generate fluorescence.

In vivo CEST MRI

An anatomical MR image showed the location of the U87 glioma (Figure 4a). The CEST MR image contrast before and after the administration of the PARACEST agents was used to determine the dynamic change in % CEST during the study (Figure 4b). Based on image noise, a CEST effect of ≥5.2% had a 95% probability that the CEST effect was real. The MR images prior to injection showed no significant CEST effect, but this significance threshold was exceeded immediately after injection of the agent. A strong CEST effect was first visualized at the tumor rim 2.8 min after injection, which can be attributed to the hypervascular rim typically observed in malignant glioma tumors [26]. The CEST effect persisted during the remainder of the MRI study, which was attributed to the enhanced permeability and retention effect that is typically observed with nano-sized agents in glioma tumors [27]. For comparison, the contralateral brain tissue did not show a statistically significant CEST effect throughout the MRI scan session. The temporal results shown in Figure 4C demonstrate variability in the baseline measurement prior to injection, which was attributed to pulse imperfections. This variability was greater after injection of the agent, which was attributed to motion artifacts (despite the use of a stereotactic holder) and pulse imperfections. This 'noise' in Figure 4C has been observed in similar *in vivo* CEST MRI studies [7,8,13,17]. This result indicated that CEST MRI could detect the presence of the dual-modality contrast agent in the glioma, which detected the glioma with excellent specificity, relative to normal brain tissue.

This experimental approach only required the acquisition of CEST MR images at one saturation frequency, which simplified the acquisition method relative to approaches that require multiple saturation frequencies. This approach also accounted for static effects that influence the contrast of a MR image with selective saturation, including endogenous magnetization transfer, direct saturation of water, and B0 and B1 magnetic field inhomogeneities. However, the use of one saturation frequency cannot account for other dynamic changes caused by the agent. For example, macrocyclic Eu(III) chelates have recently been shown to have a significant T2ex rate that can cause dynamic darkening of the image [21]. Although Eu(III) chelates have very low T1 relaxivities, the high ratio of Eu(III) chelates per dendrimer may compensate for low T1 relaxivity and may possibly cause a change in image contrast. Yet the statistically significant, dynamic changes in image contrast after injection still ensure that the MRI method detected the agent.

To elucidate the influence of T1, T2ex, magnetic susceptibilities and magnetization transfer on CEST MRI, a complimentary analysis method is needed that can accurately determine the concentration of the agent without also being influenced by these other physicochemical effects. Biosensor imaging of redundant deviation in shifts (BIRDS) has been used to detect lanthanide chelates using chemical shift imaging, and has outstanding potential to provide this complimentary analysis to further evaluate CEST [34]. BIRDS has been employed to simultaneously measure temperature and pH during a single *in vivo* study, which provides additional information that may improve biomedical diagnoses [35,36]. BIRDS chemical-shift imaging and CEST MRI studies have not yet been demonstrated in the same *in vivo* system. As described below, including fluorescence imaging may compliment or validate future BIRDS chemical-shift imaging–CEST MRI studies.

In vivo & *ex vivo* optical imaging

Macroscopic fluorescence imaging validated that the CEST MRI results were generated by accumulation of the dual-modality contrast agent in the glioma. *In vivo* fluorescence imaging showed accumulation of the contrast agent in the brain (Figure 5a). The comparison of *ex vivo* fluorescence imaging (Figure 5b) and the anatomical MR image (Figure 5C) further confirmed that the accumulation occurred in the glioma tumor (Figure 5d). The *ex*

vivo study may also have been accomplished by detecting the fluorescence from Eu(III) in the chelate. However, Eu(III) chelates typically have weak fluorescence, so the *in vivo* study would have been difficult to accomplish, based on Eu(III) fluorescence [37]. Therefore, we elected to use the DyLight 680 fluorophore for the *in vivo* and *ex vivo* studies for consistency.

The specificity of *in vivo* CEST MRI for glioma detection was further validated with *ex vivo* fluorescence microscopy, which showed that the contrast agent accumulated in the glioma tumor, but not in the contralateral brain tissue (Figure 6a & 6b). Fluorescence microscopy at micrometer spatial resolution was conducted following lectin staining, which identified vessel lumen and DAPI staining that identified viable cellularity (Figure 6C–F). The multicolor microscopy images of the glioma showed that the contrast agent extravasated across the vessel lumen. Microscopy images of the contralateral tissue showed that the agent remained in the vessel lumen and did not extravasate into normal brain tissues. This result provides a plausible rationale for the persistence of the CEST effect in the glioma during the *in vivo* MRI study, which further validates the *in vivo* CEST MRI result. This result also demonstrates the advantages of using a nano-sized dendrimer when developing new imaging agents detecting gliomas.

Merits of dual-modality imaging

The *in vivo* and *ex vivo* imaging of the dual-modality contrast agent showed excellent potential utility for identifying the location of gliomas. *In vivo* CEST MRI immediately following injection of the agent highlighted the hypervascular rim of the tumor (Figure 4b, at the 10.8-min time-point), which was similar but not identical to the location of the tumor rim identified by the anatomical MR image (Figure 4a). This result indicates that CEST MRI may provide a more sensitive diagnosis of the hypervascular rim of the tumor than the anatomical image, which demonstrates the merits of using an exogenous contrast agent for glioma detection. The persistence of the CEST MRI contrast throughout the glioma contributed to the identification of the tumor location at a millimeter scale.

In vivo and *ex vivo* fluorescence imaging also showed the location of the tumor, which demonstrated that similar intrasurgical fluorescence imaging with a wide-field view may improve sensitivity for detecting tumor locations at a millimeter scale. The high-resolution *ex vivo* fluorescence imaging demonstrated that similar intrasurgical fluorescence imaging may detect tumor features at a micrometer scale. Thus, a PARACEST-fluorescence imaging contrast agent offers potential to diagnose gliomas at multiple spatial scales, before and during surgical resection of gliomas and other pathological tissues.

Future perspective

This study demonstrates the merits of using a PAMAM dendrimer as a nanocarrier for imaging contrast agents. In the future, this approach can be exploited to improve the specificity for detecting glioma by using a nano-sized imaging contrast agent. This study also demonstrates the merits of dual-modality imaging contrast agents conjugated to a single dendrimer for cross-validation of results and for detecting pathological tissues at different spatial scales, which may be exploited in future studies as a short-term goal, and may be translated to the clinic as a long-term goal. Finally, this study demonstrated that *in vivo* CEST MRI is feasible with PARACEST agents conjugated to a dendrimer.

To relate this study to the authors' previous research, they used a common Eu(III) macrocyclic chelate. Future studies may employ other types of PARACEST agents that are responsive to tumor biomarkers such as tumor acidosis, protease enzyme activities or metabolites, which would provide additional diagnostic specificity for gliomas.

Additionally, future studies may conjugate multiple types of PARACEST agents on a single dendrimer to detect multiple biomarkers of pathological tissues that will further improve diagnostic specificity. This study demonstrates the modular nature of conjugating PARACEST agents to a PAMAM dendrimer. Therefore, this study represents a milestone in the development of dual-modality, nano-sized contrast agents that can be detected with CEST MRI and optical imaging.

Conclusion

In conclusion, the authors have developed a dual-modality imaging contrast agent that used a PAMAM dendrimer to carry a PARACEST agent and a fluorescent tag. The PARACEST and fluorophore agents were each unaffected by the other agents on the dendrimer. *Invivo* CEST MRI detected the agent in a glioma model but not in contralateral tissue, and the specificity of the agent for the glioma was validated with *in vivo* and *ex vivo* fluorescence imaging and fluorescent microscopy. The *in vivo* CEST MRI showed the macroscopic location of the tumor including the hypervascular rim, while fluorescence imaging showed the microscopic location of the agent in the tissues, which demonstrated that, the dual-modality contrast agent has utility at different spatial scales.

References

Papers of special note have been highlighted as:

■ of interest

■■ of considerable interest

1. Merbach, AE.; Toth, E. The chemistry of contrast agents in medical MRI. John Wiley & Sons; NY, USA: 2001. p. 45-120.
2. Lavis LD, Raines RT. Bright ideas for chemical biology. ACS Chem Biol. 2008; 3(3):142–155. [PubMed: 18355003]
3. Zhang S, Merritt M, Woessner DE, Lenkinski RE, Sherry AD. PARACEST agents: modulating MRI contrast via water proton exchange. Acc Chem Res. 2003; 36(10):783–790. [PubMed: 14567712]

4■■. Ward KM, Aletras AH, Balaban RS. A new class of contrast agents for MRI based on proton chemical exchange dependent saturation transfer (CEST). J Magn Reson. 2000; 143(1):79–87. Seminal publication introduces chemical exchange saturation transfer (CEST) MRI contrast agents. [PubMed: 10698648]

5■■. Zhang S, Winter P, Wu K, Sherry AD. A novel Europium(III)-based MRI contrast agent. J Am Chem Soc. 2001; 123(7):1517–1518. Introduces paramagnetic CEST (PARACREST) agents. [PubMed: 11456734]

6. Aime S, Barge A, Delli Castelli D, et al. Paramagnetic lanthanide(III) complexes as pH-sensitive chemical exchange saturation transfer (CEST) contrast agents for MRI applications. Magn Reson Med. 2002; 47(4):639–648. [PubMed: 11948724]
7. Liu G, Li Y, Sheth VR, Pagel MD. Imaging *in vivo* extracellular pH with a single PARACEST MRI contrast agent. Mol Imaging. 2012; 11(1):47–57. [PubMed: 22418027]
8. Sheth VR, Li Y, Chen LQ, Howison CM, Flask CA, Pagel MD. Measuring *in vivo* tumor pHe with CEST–FISP MRI. Magn Reson Med. 2012; 67(3):760–768. [PubMed: 22028287]

9■. Yoo B, Pagel MD. A PARACEST MRI contrast agent to detect enzyme activity. J Am Chem Soc. 2006; 128(43):14032–14033. Reports the first demonstration of a responsive CEST agent. [PubMed: 17061878]

10. Chauvin T, Durand P, Bernier M, et al. Detection of enzymatic activity by PARACEST MRI: a general approach to target a large variety of enzymes. Angew Chem Int Ed. 2008; 47(23):4370–4372.

11. Suchý M, Ta R, Li AX, et al. A paramagnetic chemical exchange-based MRI probe metabolized by cathepsin D: design, synthesis and cellular uptake studies. Org Biomol Chem. 2010; 8(11):2560–2566. [PubMed: 20485791]
12. Liu G, Li Y, Pagel MD. Design and characterization of new irreversible responsive PARACEST MRI contrast agent that detects nitric oxide. Magn Reson Med. 2007; 58(6):1249–1256. [PubMed: 18046705]
13■■. Ali MM, Liu G, Shah T, Flask CA, Pagel MD. Using two chemical exchange saturation transfer magnetic resonance imaging contrast agents for molecular imaging studies. Acc Chem Res. 2009; 42(7):915–924. First demonstration of selectively detecting two PARACEST agents during a single CEST MRI scan session. [PubMed: 19514717]
14. Li AX, Hudson RHE, Barrett JW, Jones CK, Pasternak SH, Bartha R. Four-pool modeling of proton exchange processes in biological systems in the presence of MRI–paramagnetic chemical exchange saturation transfer (PARACEST) agents. Magn Reson Med. 2008; 60(5):1197–1206. [PubMed: 18958857]
15■. Vinogradov E, He H, Lubag A, Balschi JA, Sherry AD, Lenkinski RE. MRI detection of paramagnetic chemical exchange effects in mice kidneys *in vivo*. Magn Reson Med. 2007; 58(4): 650–655. First demonstration of *in vivo* 'on resonance' CEST MRI. This method has improved sensitivity relative to 'off resonance' CEST MRI, but can only detect one PARACEST agent during the MRI scan session. [PubMed: 17899603]
16■. Liu G, Ali M, Yoo B, Griswold MA, Tkach JA, Pagel MD. PARACEST MRI with improved temporal resolution. Magn Reson Med. 2009; 61(2):399–408. First demonstration of *in vivo* 'off resonance' CEST MRI. This method can selectively detect multiple PARACEST agents during a single MRI scan session. [PubMed: 19165903]
17. Ali MM, Yoo B, Pagel MD. Tracking the relative *in vivo* pharmacokinetics of nanoparticles with PARACEST MRI. Molec Pharm. 2009; 6(5):1409–1416. [PubMed: 19298054]
18. Jones CK, Li AX, Suchy M, Hudson RHE, Menon RS, Bartha R. *In vivo* detection of PARACEST agents with relaxation correction. Magn Reson Med. 2010; 63(5):1184–1192. [PubMed: 20432289]
19. Li AX, Suchy M, Li C, et al. *In vivo* detection of MRI-PARACEST agents in mouse brain tumors at 9.4 T. Magn Reson Med. 2011; 66(1):67–72. [PubMed: 21254213]
20. Delli Castelli D, Dastru W, Terreno E, et al. *In vivo* MRI multicontrast kinetic analysis of the uptake and intracellular trafficking of paramagnetically labeled liposomes. J Control Rel. 2010; 144(3):271–279.
21. Soesbe TC, Togao O, Takahashi M, Sherry AD. SWIFT-CEST: a new MRI method to overcome T2 shortening caused by PARACEST contrast agents. Magn Reson Med. 2011 (Epub ahead of print). 10.1002/mrm.23302
22. Pikkemaat JA, Wegh RT, Lamerichs R, et al. Dendritic PARACEST contrast agents for magnetic resonance imaging. Contrast Media Mol Imaging. 2007; 2(5):229–239. [PubMed: 17937448]
23. Wu Y, Zhou Y, Ouari O, et al. Polymeric PARACEST agents for enhancing MRI contrast sensitivity. J Am Chem Soc. 2008; 130(42):13854–13855. [PubMed: 18817395]
24. Vasalatiy O, Gerard RD, Zhao P, Sun X, Sherry AD. Labeling of adenovirus particles with PARACEST agents. Bioconj Chem. 2008; 19(3):598–606.
25. Pagel MD. The hope and hype of multimodality imaging contrast agents. Nanomedicine. 2011; 6(6):945–948. [PubMed: 21955073]
26. Tovi M. MR imaging in cerebral gliomas analysis of tumor tissue components. Acta Radiol. 1993; 384:1–24.
27. Gioux S, Choi HS, Frangioni JV. Image-guided surgery using invisible near-infrared light: fundamentals of clinical translation. Molec Imaging. 2010; 9(5):237–255. [PubMed: 20868625]
28. Fujimaki T. Central nervous system germ cell tumors: classification, clinical features, and treatment with a historical overview. J Child Neurol. 2009; 24(11):1439–1445. [PubMed: 19841431]
29. Matsumura Y, Maeda H. A new concept for macromolecular therapeutics in cancer chemotherapy: mechanism of tumoritropic accumulation of proteins and the antitumor agent smancs. Cancer Res. 1986; 46(12 Pt 1):6387–6392. [PubMed: 2946403]

30. Sarin H, Kanevsky AS, Wu H, et al. Effective transvascular delivery of nanoparticles across the blood–brain tumor barrier into malignant glioma cells. J Trans Med. 2008; 6:80–84.

31. Ali MM, Janic B, Babajani-Feremi A, et al. Changes in vascular permeability and expression of different angiogenic factors following anti-angiogenic treatment in rat glioma. PLoS ONE. 2010; 15(1):1–10.

32. Zhang S, Winter P, Wu K, Sherry AD. A novel europium(III)-based MRI contrast agent. J Am Chem Soc. 2001; 123(7):1517–1518. [PubMed: 11456734]

33. Valeur, B. Molecular fluorescence. principles and applications. Wiley VCH; Weinheim, Germany: 2002. p. 34-71.

34. Coman D, Kiefer GE, Rothman DL, Sherry AD, Hyder F. A lanthanide complex with dual biosensing properties: CEST (chemical exchange saturation transfer) and BIRDS (biosensor imaging of redundant deviation in shifts) with europium DOTA-tetraglycinate. NMR Biomed. 2011; 24(10):1216–1225. [PubMed: 22020775]

35. Coman D, Trubel HK, Rycyna RE, Hyder F. Brain temperature and pH measured by 1H chemical shift imaging of a thullium agent. NMR Biomed. 2009; 22(2):229–239. [PubMed: 19130468]

36. Coman D, Trubel HK, Hyder F. Brain temperature by biosensor imaging of redundant deviation in shifts (BIRDS): Comparison between Tm DOTP5- and TmDOTMA- NMR Biomed. 2010; 23(3): 277–285. [PubMed: 19957287]

37. Josan JS, De Silva CR, Yoo B, et al. Fluorescent and lanthanide labeling for ligand screens, assays, and imaging. Methods Mol Biol. 2011; 716:89–126. [PubMed: 21318902]

Executive summary

- A dual-modality, paramagnetic chemical exchange saturation transfer-fluorescence imaging contrast agent has been developed by using a generation 5 polyamidoamine dendrimer as a nano-sized carrier.
- The presence of each contrast agent on the dendrimer did not affect the detection sensitivity of the other contrast agent.
- The nano-sized contrast agent facilitated *in vivo* chemical exchange saturation transfer MRI.
- *In vivo* and *ex vivo* fluorescence imaging validated the *in vivo* chemical exchange saturation transfer MRI results.
- The dual-modality imaging contrast agent detected the glioma with high specificity at different spatial scales.

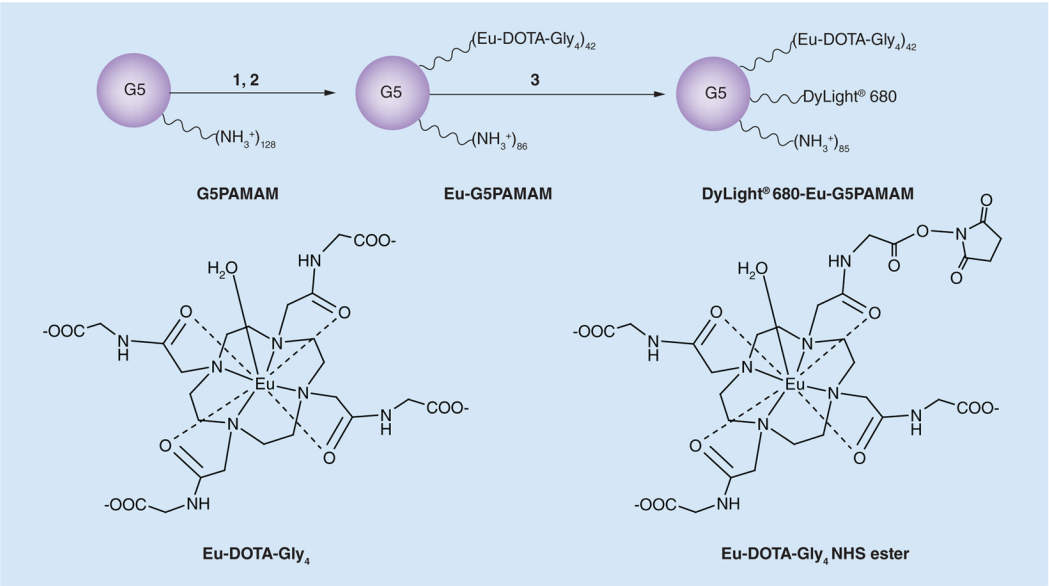

Figure 1. Synthesis of the dual-modality contrast agent

(**1**) Eu-DOTA-Gly_4, NHS (1.8 equivalents), EDC (4.5 equivalents), 2-(*N*-morpholino)ethanesulfonic acid, pH 6.5, 0°C, 1 h; **(2)** G5 (0.072 equivalent), phosphate-buffered saline, pH 7.4, room temperature, 24 h; 37% yield (42 Eu-DOTA-Gly_4 units among 128 NH_3^+ polyamidoamine chain termini); **(3)** 2 (70 μmol), DyLight® 680 NHS ester (1 equivalent), phosphate-buffered saline, room temperature, 24 h, 93% yield. The average stoichiometry is listed for each ligand. The chemical exchange saturation transfer effect arises from the bound water of Eu-DOTA-Gly_4.

EDC: 1-ethyl-3-(3-dimethylaminopropyl) carbodiimide; Eu-DOTA-Gly_4: Eu-1,4,7,10-tetraazacclododecane-1,4,7,10-tetraacetic acid-Gly_4; G5: G5PAMAM; G5PAMAM: Generation 5 polyamidoamine; NHS: *N*-hydroxysuccinimide.

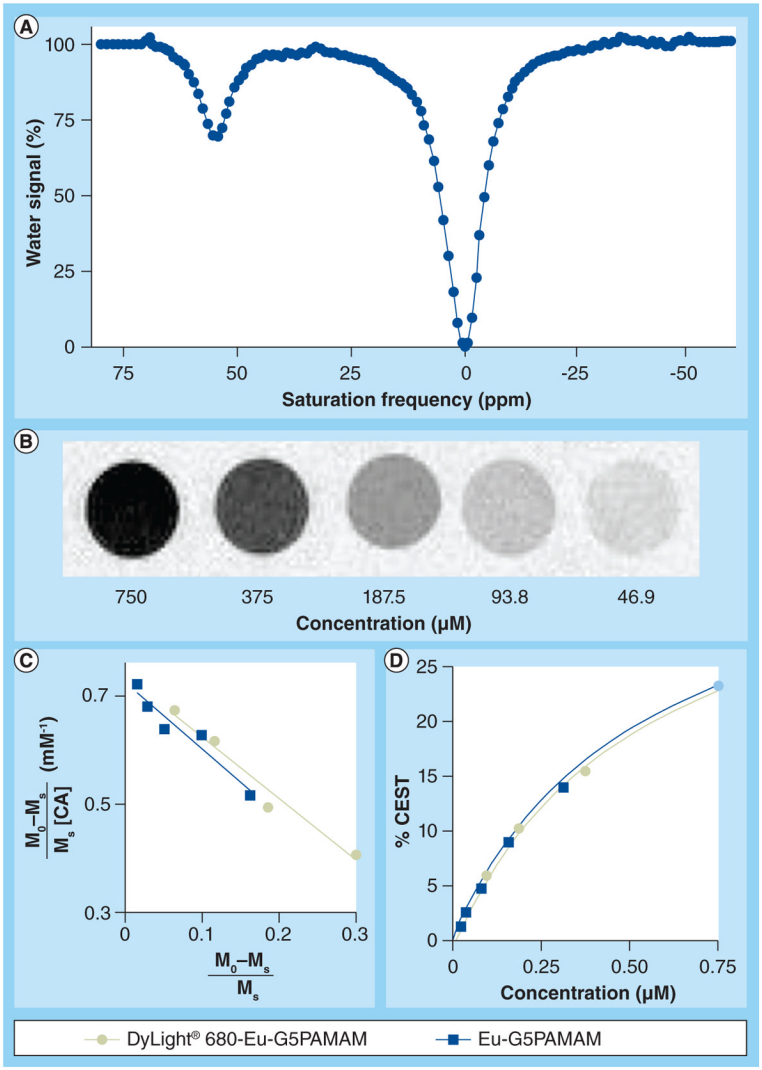

Figure 2. The chemical exchange saturation transfer effect of DyLight 680-Eu-generation 5 polyamidoamine

(A) The spectrum shows a CEST effect at +55 ppm. **(B)** The CEST MR images of DyLight® 680-Eu-G5PAMAM show a contrast dependence on concentration. **(C)** A Hanes-like linear analysis method shows that CEST of DyLight 680-Eu-G5PAMAM fits a two-pool model, Hanes-like fitting shown as a green line). For comparison, the Hanes-line analysis of Eu-G5PAMAM as reported in [17] is also shown. **(D)** The CEST dependence on concentration determined from the Hanes-like analysis for DyLight 680-Eu-G5PAMAM and Eu-G5PAMAM as reported in [17] are the same (the green line exactly overlays on the blue line).

CA: Contrast agent; CEST: Chemical exchange saturation transfer; G5PAMAM: Generation 5 polyamidoamine; M0: Selective saturation at −55 ppm; Ms: Selective saturation at +55 ppm.

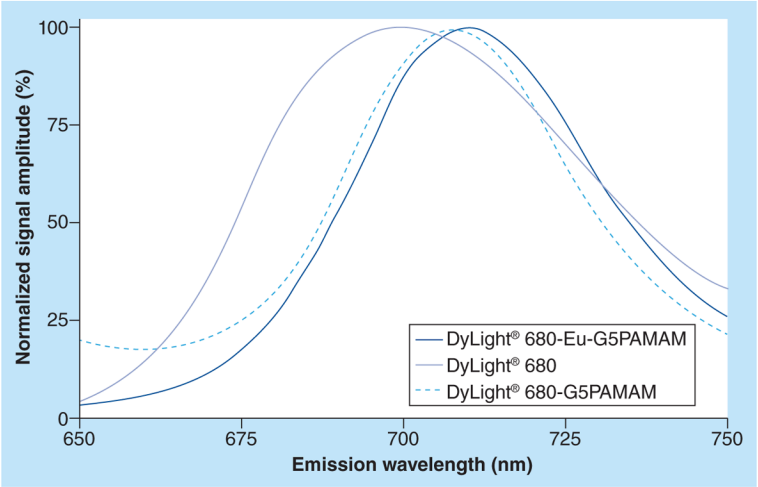

Figure 3. Emission fluorescence spectra

Conjugation of Dylight® 680 to the G5PAMAM dendrimer caused a 10-nm red shift in the maximum emission wavelength. The dual-modality contrast agent DyLight 680-Eu-G5PAMAM also showed a 10-nm red shift, which demonstrated that the presence of the PARACEST agent on the dendrimer did not effect the emission wavelength.

G5PAMAM: Generation 5 polyamidoamine; PARACEST: Paramagnetic chemical exchange saturation transfer.

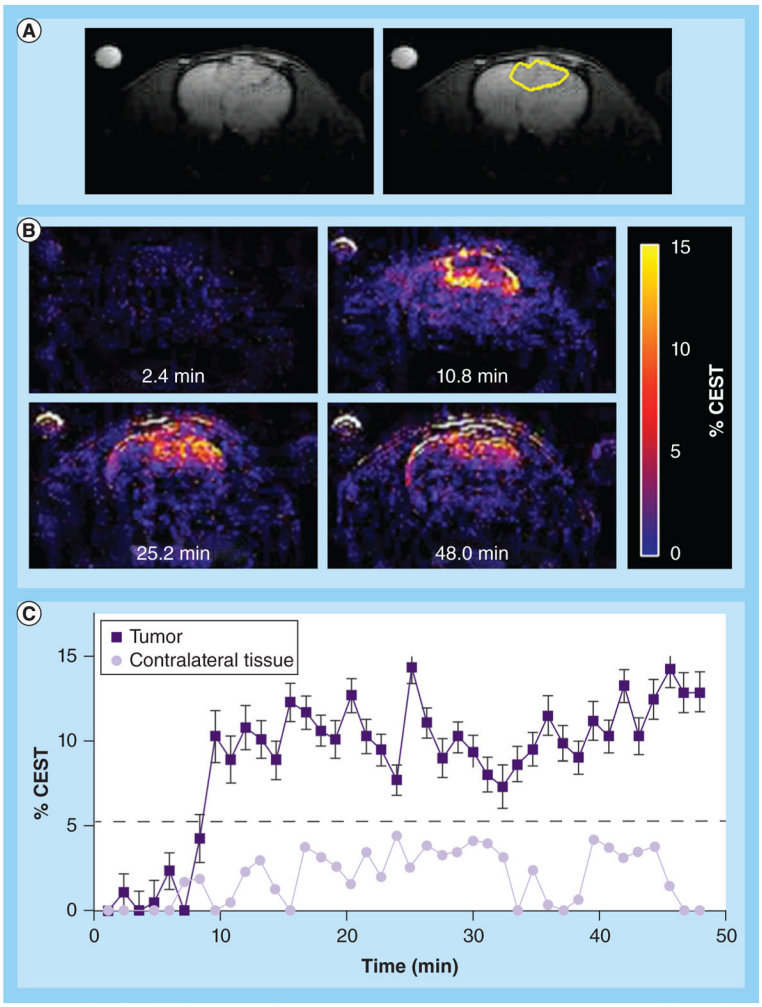

Figure 4. ***In vivo*** **chemical exchange saturation transfer MRI**

(A) The left panel shows an anatomical image that identifies the location of the tumor prior to administration of the agent. The right panel highlights the location of the tumor. **(B)** Paramagnetic CEST maps detected the agent in the U87 tumor but not in the contralateral tissue. The maps are labeled with the time-point relative to injection. **(C)** The temporal change in CEST shows rapid accumulation and persistence of the agent in the U87 tumor. CEST was greater than the 95% probability threshold in the U87 tumor, but was less than the probability threshold for the contralateral tissue.

CEST: Chemical exchange saturation transfer.

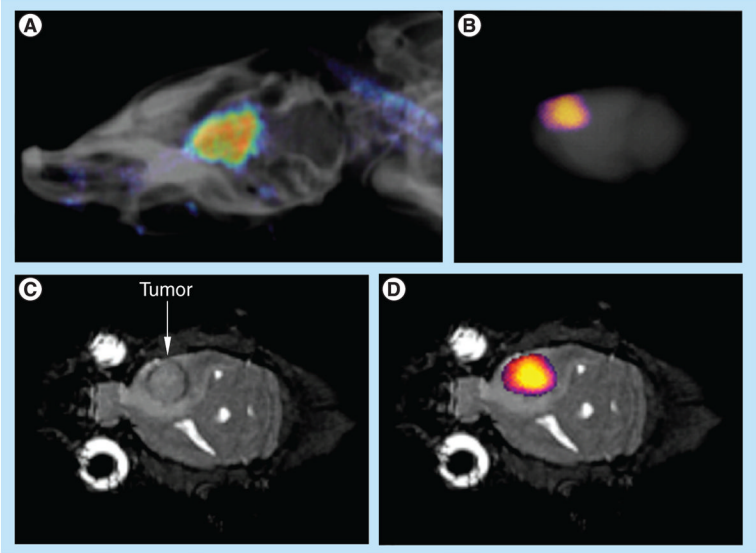

Figure 5. Macroscopic fluorescence imaging

(A) The *in vivo* fluorescent image of the rat head overlayed on an x-ray image shows the presence of the agent in the U87 tumor in the brain. **(B)** The *ex vivo* fluorescence image of the whole brain also detected the agent in the brain (fluorescent image was overlayed on x-ray image of the whole brain). **(C)** The coronal MRI shows the location of the U87 tumor. **(D)** The *ex vivo* fluorescence image was also overlayed on the MRI to show that the agent was located in the U87 glioma. The anatomy of the brain was correlated between MRI and x-ray images.

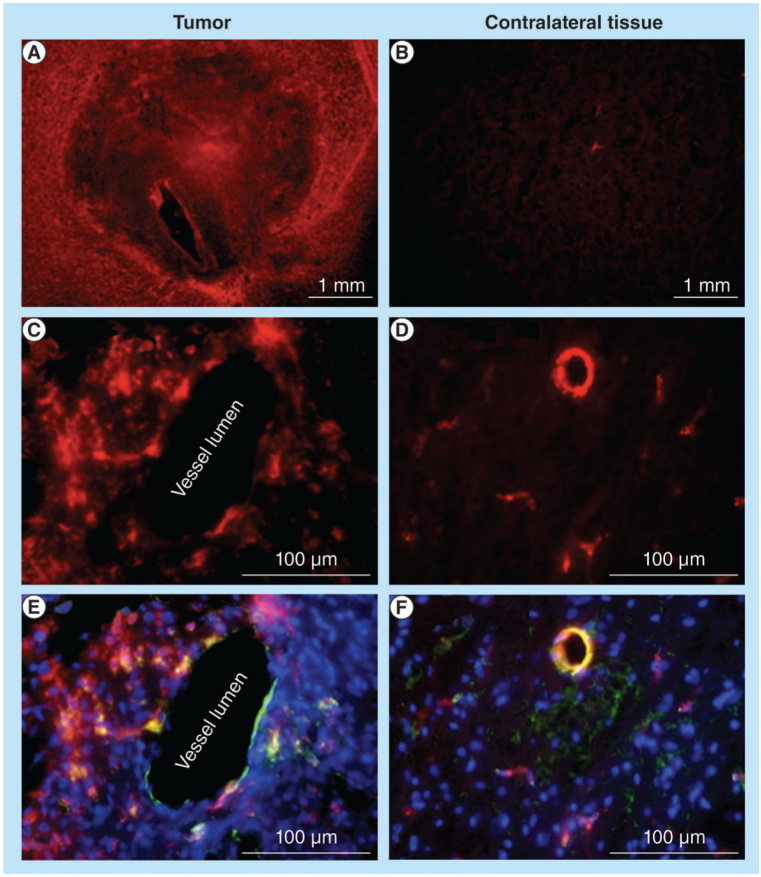

Figure 6. Microscopic fluorescence imaging

(A) Strong, pervasive distribution of the agent was visualized in tumor tissue. **(B)** Weak, focal distribution was visualized in the contralateral tissue. **(C)** A high-resolution view showed that the agent extravasated across the endothlium in tumor tissue, **(D)** but not in contralateral tissue. **(E & F)** Overlays of fluorescence from the agent, lectin staining of endothelium and 4′,6-diamidino-2-phenylindole staining for viable cellularity, validated the spatial distribution of the agents observed in **C & D**. The exposure time for tumor area and contralateral brain was kept identical. The images of **D & F** were enhanced to show fluorescent activity in the vessels.